INTERNATIONAL JOURNAL FOR NUMERICAL METHODS IN FLUIDS, VOL. 11, 127–150 (1990)

CONVERGENCE STUDIES WITH THE SANDIA OCEAN MODELING SYSTEM

DAVID E. DIETRICH AND PATRICK J. ROACHE

Ecodynamics Research Associates, PO Box 8172, Albuquerque, NM, U.S.A.

AND

MEL G. MARIETTA

Sandia National Laboratories, Albuquerque, NM 87185, U.S.A.

SUMMARY

Five numerical schemes are compared using convergence studies in the framework of the hydrostatic Sandia Ocean Modeling System (SOMS). Three resolutions are used, 40, 20 and 10 km, with respectively three, seven and 15 layers and time steps of 60, 30 and 15 min, so 15 convergence calculations are performed. The same geophysical prototype problem (exhibiting baroclinic instability in a statically stable environment) is used for all calculations.

All five schemes are second-order-accurate in space, but those using four-point interpolations for the Coriolis and pressure gradient terms are shown to produce much more accurate results, with relatively little extra computation, than schemes using two-point interpolations.

Convergence is also indicated with decreasing horizontal diffusivities of 10^7, 10^6, and 10^5 $cm^2 s^{-1}$. Using 10^7 $cm^2 s^{-1}$ diffusivities causes substantial damping of the dominant instabilities during the 30-day integrations performed, but using 10^6 $cm^2 s^{-1}$ results in little damping and yields results very close to those using 10^5 $cm^2 s^{-1}$.

A barotropic (vertically averaged flow) cyclonic northern basin gyre is explained as a weakly forced circulation. Its equilibrium amplitude is determined by a balance between dissipation effects due to horizontal mixing and diffusion, and weak second-order driving associated with thermodynamic forcing and vorticity dissipation at the basin bottom. It is thus quite sensitive to model dissipation but can be well described by SOMS owing to SOMS' low numerical dissipation.

KEY WORDS Ocean model Grid convergence Energy conservation

1. INTRODUCTION

The Sandia Ocean Modeling System (SOMS)[1] is being used to address a large range of geophysical phenomena, including lake circulations,[2] bottom boundary layer phenomena on the continental slope,[3] open ocean flow over a seamount[4] and the general circulation of the North Atlantic Ocean with real topography.[5]

Although the original SOMS performs well with these problems, we have recently substantially improved its numerical integration of the Coriolis terms by using the higher-order (using four points instead of two) interpolation schemes for the Coriolis terms described in Section 3. We have also implemented a corresponding higher-order interpolation scheme for the pressure gradient terms on a semi-collocated grid, as described in Section 3. In this paper these various

0271–2091/90/100127–24$12.00

Received 18 May 1989
Revised 25 August 1989

versions of SOMS (five in all) are applied to two important calculation sequences using the geophysical prototype test problem described in Section 2.

The first sequence decreases viscosity with everything else fixed (Section 4.1). This is especially relevant to geophysical flows owing to their nearly inviscid nature (most of their energy is contained in large-scale motions for which the appropriate subgrid-scale eddy Reynolds number is very large) and is needed to compare computed free-mode eddy scales with those predicted by inviscid stability theory.

The second sequence increases resolution with everything else fixed (Section 4.2). Model credibility requires convergence with increasing resolution.

2. THE TEST PROBLEM

The geophysical prototype test problem described below is used to investigate the effects of variable eddy diffusivity (Section 4.1) and resolution (Section 4.2).

In choosing a test problem it is prudent to avoid convective (Rayleigh–Taylor) instability that occurs when denser fluid lies directly above less dense fluid. The large difference in scales between eddies due to convective instability and those due to baroclinic instability (associated with horizontal density gradients, leading to large atmospheric and oceanic eddies) would require very high resolution to converge in a problem with both instabilities present. Although convective adjustment schemes avoid direct modelling of convectively unstable modes, our goals herein do not include showing convergence of convective adjustment schemes. These considerations led to the following test problem.

The test problem is a fully insulated flat-bottom rectangular basin with dimensions 600 km by 480 km by 3·75 km deep. Free-slip conditions are applied everywhere except at the top surface, where a wind stress is applied. No external heating is added. A baroclinic, stratified initial state drives the flow from an initial state of rest. Constant horizontal heat and momentum eddy transfer coefficients are assumed. Constant vertical heat and momentum eddy transfer coefficients of 10 and 20 $cm^2 s^{-1}$ are used for all cases. The initial velocity is zero everywhere. The initial top layer temperature is 16 °C at the southern boundary and 13 °C at the northern boundary. The initial bottom layer temperature is 5 °C everywhere. The initial temperature is also linearly stratified between the specified top and bottom temperatures.

Finally, the surface wind stress is a single-gyre pattern (a half-wavelength sine wave with amplitude 0·125 dyn cm^{-2} and zero at mid-latitude) but has a secondary effect compared to the initial buoyancy.

This test problem is clearly not a pure stability problem. The side boundaries force finite amplitude zonal variations immediately. This is characteristic of the real ocean near the western boundary separation, except that the 'side' boundary is only one-sided in the real ocean. Our goal is to show model credibility using a problem with much of the physics of the real ocean, albeit with different geometic constraints.

3. NUMERICAL APPROACHES

Five numerical methods are used for the test problem. Four use the Arakawa 'c' staggered grid[6] (Figure 1), as does the original SOMS method.[1] This means the momentum conservation equations are integrated in control volumes that are staggered with respect to the control volumes for other variables. The fifth method uses a collocated grid in which all control volumes are collocated, although a non-divergent advection velocity is determined at the 'c'-grid staggered locations for improved accuracy and conservation properties.

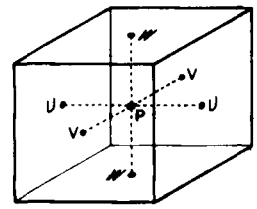

Figure 1. Arakawa 'c' staggered grid: single control volume for pressure (P). The symbol P denotes the centre of the P-control volume. The symbols U, V and W illustrate relative positions of control volume centres for longitudinal, latitudinal and vertical velocities

We now describe the five schemes with reference to simplified equations. Since the distinguishing features of the methods concern only the time derivative terms, the Coriolis terms and the vertical diffusion terms of the momentum equations, the remaining terms are grouped into U and V and the simplified momentum equations are

$$\begin{aligned} \partial u/\partial t &= U + f*v + uz, \\ \partial v/\partial t &= V - f*u + vz, \end{aligned} \tag{1}$$

where uz and vz are the vertical diffusion terms and f is the Coriolis parameter factor in the Coriolis acceleration terms, which varies only with latitude.

3.1. Scheme 1A

This is the SOMS algorithm described in Reference 1. The procedure is as follows.

1. Calculate the term $U(i,j)$ and $V(i,j)$ in the following schematic representation of the staggered (see Figure 1) control volume equations:

$$\begin{aligned} u(i+1/2,j,k,n+1) &= u(i+1/2,j,k,n) + \Delta t*[U(i+1/2,j,k) + f*v + uz], \\ v(i,j+1/2,k,n+1) &= v(i,j+1/2,k,n) + \Delta t*[V(i,j+1/2,k) - f*u + vz]. \end{aligned} \tag{2}$$

   The terms U and V are integrated explicitly (in time).

2. Interpolate the explicit terms U and V and the old time level u- and v-velocity components to the p-locations using simple two-point centred averages:

$$\begin{aligned} U(i,j,k) &= [U(i+1/2,j,k) + U(i-1/2,j,k)]/2, \\ V(i,j,k) &= [V(i,j+1/2,k) + V(i,j-1/2,k)]/2, \\ u(i,j,k,n) &= [u(i+1/2,j,k,n) + u(i-1/2,j,k,n)]/2, \\ v(i,j,k,n) &= [v(i,j+1/2,k,n) + v(i,j-1/2,k,n)]/2. \end{aligned} \tag{3}$$

3. Integrate the full equations, including the implicitly coupled Coriolis and vertical diffusion terms, at the p-locations:

$$\begin{aligned} u(i,j,k,n+1) &= u(i,j,k,n) + \Delta t*[U(i,j,k) + f*v(i,j,k,n+1) + uz(i,j,k,n+1)], \\ v(i,j,k,n+1) &= v(i,j,k,n) + \Delta t*[V(i,j,k) - f*u(i,j,k,n+1) + vz(i,j,k,n+1)]. \end{aligned} \tag{4}$$

   Note that the same (backward in this case) implicit scheme must be used for both Coriolis and vertical diffusion terms to get accurate, efficient boundary layer modelling.[1]

4. Interpolate the results from step 3 back to the staggered u- and v-locations:

$$u(i+1/2,j,k,n+1) = [u(i,j,k,n+1) + u(i+1,j,k,n+1)]/2,$$
$$v(i,j+1/2,k,n+1) = [v(i,j,k,n+1) + v(i,j+1,k,n+1)]/2. \tag{5}$$

5. Clear out the divergence of the barotropic mode (vertically averaged horizontal flow) by solving a two-dimensional Poisson equation for the surface pressure correction 'dp' [1,7] correcting the pressure gradient in the terms U and V in equation (2) and adding the effects of the corrected pressure gradient (the correction is independent of depth) everywhere to the new u- and v-velocity components:

$$u(i+1/2,j,k,n+1) = u(i+1/2,j,k,n+1) + \Delta t * [dp(i+1,j) - dp(i,j)],$$
$$v(i,j+1/2,k,n+1) = u(i,j+1/2,k,n+1) + \Delta t * [dp(i,j+1) - dp(i,j)]. \tag{6}$$

This adjustment is performed explicitly without implicit coupling to Coriolis terms. Step 3 already included an implicit response to the pressure gradient terms (in the explicitly integrated terms U and V). When the time step is small compared to an inertial period ($2\pi/f$), the implicit response to the pressure gradient increments is similar to the explicit calculation in equation (6). Further, gradients of the pressure increments 'dp' are small compared to the pressure gradients included in the terms U and V in step 3. Thus, although implicit responses to 'dp' could be included by iterating steps 2–5 within a time step, such a procedure has only a very secondary effect.

With the explicit treatment of the Coriolis and vertical diffusion terms, as often used, the barotropic mode divergence could be eliminated by precalculating the appropriate top layer pressure at the start of a time step from a simple two-dimensional Poisson equation corresponding to the one used in step 5 of the current procedure. For a given size of time step, the current procedure is probably more accurate than explicit treatment of these terms, since it at least includes an implicit response to a major part of the pressure gradient. However, as noted in Reference 1, the main motivation for this implicit treatment is for accurate, efficient integration of the boundary layer equations.

6. Calculate the vertical velocity by integrating the incompressibility equation.
7. Apply the 'filtered leapfrog' updating scheme described in Reference 8 to start the next time step.

This scheme has truncation error $O[(\Delta x)^2, \Delta t, (\Delta x)^2/\Delta t)]$;[1,8] thus it becomes very inaccurate for small Δt. This is due to the fact that the successive interpolations in steps 2 and 4 create unphysical signal propagation at each time step, independent of the time step size (even for $\Delta t = 0$), while all other effects are proportional to Δt. The method thus belongs to the same 'diffusing' class as the Lax method (e.g. see Reference 9, pp. 242–244). Thus the spurious effects of the interpolations increase as Δt decreases.

To avoid this peculiar behaviour, Scheme 2A was developed.

3.2. Scheme 2A

Whereas Scheme 1A interpolates velocities to the staggered 'c'-grid locations in step 4, producing a diffusive effect, the new Scheme 2A interpolates not velocities but only part of the time derivatives. Steps 1–3 of Scheme 2A are identical to those of Scheme 1A (see Section 3.1). Step 4 of Scheme 1A is replaced by the following three steps.

4a. Calculate Δu and Δv as follows:

$$\begin{aligned} \Delta u(i,j,k) &= u(i,j,k,n+1) - u(i,j,k,n) - \Delta t * U(i,j,k), \\ \Delta v(i,j,k) &= v(i,j,k,n+1) - v(i,j,k,n) - \Delta t * V(i,j,k). \end{aligned} \tag{7}$$

The term Δu and Δv approximate the changes of u and v that would result at the p-locations if the explicit terms U and V were zero, and thus represent changes due only to the implicit Coriolis and vertical diffusion terms.

4b. Interpolate Δu and Δv back to the staggered u- and v-locations:

$$\begin{aligned} \Delta u(i+1/2,j,k) &= [\Delta u(i,j,k) + \Delta u(i+1,j,k)]/2, \\ \Delta v(i,j+1/2,k) &= [\Delta v(i,j,k) + \Delta v(i,j+1,k)]/2. \end{aligned} \tag{8}$$

4c. Calculate the new velocity components u and v at the staggered locations:

$$\begin{aligned} u(i+1/2,j,k,n+1) &= u(i+1/2,j,k,n) + \Delta u(i+1/2,j,k) + \Delta t * U(i+1/2,j,k), \\ v(i,j+1/2,k,n+1) &= v(i,j+1/2,k,n) + \Delta v(i,j+1/2,k) + \Delta t * V(i,j+1/2,k). \end{aligned} \tag{9}$$

Note that Δu and Δv represent the coupled implicit terms $\Delta t*(f*v + uz)$ and $\Delta t*(-f*u + vz)$ in equations (2).

Finally, steps 5–7 of Scheme 2A are identical to those of Scheme 1A (see Section 3.1).

This method has truncation error $O[(\Delta x)^2, \Delta t]$ and by design does not produce a diffusion effect for $\Delta t = 0$, unlike Scheme 1A. In view of the peculiar truncation error effects of Scheme 1A noted in Section 3.1, one might expect Scheme 2A to be better than Scheme 1A. However, Scheme 1A, with judiciously chosen time step size, is at least competitive with Scheme 2A, and we prefer Scheme 1A at this time (see Appendix for more detailed discussion).

3.3. Schemes 1B and 2B

To reduce the errors of interpolations in Schemes 1A and 2A (see Sections 3.1 and 3.2), Schemes 1B and 2B have been developed recently. Schemes 1B and 2B are like Schemes 1A and 2A respectively, except that the interpolations between the p-locations and the 'c'-grid staggered u- and v-locations are performed with higher accuracy. In particular, instead of interpolating the two nearest locations to the central point, a cubic is fitted through four nearby locations and the result is evaluated at the central location. For example, let four successive u-values along a latitude be $(u(i), i = 1\text{–}4)$. Then the original low-order interpolation scheme is given by

$$u(i+1/2) = [u(i) + u(i+1)]/2, \tag{10}$$

while the new higher-order interpolation scheme is given by

$$u(i+1/2) = \{9*[u(i) + u(i+1)] - [u(i-1) + u(i+2)]\}/16. \tag{11}$$

The new higher-order interpolation Schemes 1B and 2B increase accuracy and decrease spurious numerical dissipation substantially, while requiring only a few extra operations per grid point per time step. (The order of accuracy of the overall schemes remains unchanged, but the size of the error decreases. See Reference 9 for additional discussion.)

In a simple problem initialized with an eight-grid-interval eddy (16-grid-interval sine wave) and with no forcing, the effect of the interpolations using Scheme 1B is to decrease the amplitude by only about 5% per 100 time steps, while Scheme 1A leads to about 10% decrease every five steps. Thus, for this problem, the higher-order interpolation Scheme 1B leads to about 40 times less

numerical dissipation than Scheme 1A. Although Scheme 3B described below has no such dissipative interpolations, Schemes 1B and 2B are at least competitive with Scheme 3B for the geophysical prototype problem described in Section 2, and all three higher-order 'B' schemes are clearly better than the lower-order 'A' schemes for this problem.

The higher-order interpolation schemes also give better results in ocean basin-scale calculations. Schemes 1B and 2B both give a realistically stronger western boundary current than Schemes 1A and 2A in ocean basin-scale calculations,[10] with both schemes producing significant transient eddy activity.

At this time it appears that Scheme 1B is the best of the four schemes, although further analysis may be warrented.

3.4. Scheme 3B

Scheme 3B is used on the collocated grid. It differs from the original SOMS scheme in three ways: the control volumes for the momentum conservation equations are centred at the pressure locations rather than at the staggered 'c'-locations; no interpolations are used in integrating the Coriolis terms since they are collocated; and the pressure gradient terms are evaluated using a four-point difference scheme over four grid intervals. Except for diffusivities, the same advection and diffusion operators are used for all quantities, and these are identical to those given in Reference 1 for the internal energy (temperature) conservation equation.

Using the simplified equations (1), the procedure for Scheme 3B is as follows.

1. Calculate the terms $U(i,j)$ and $V(i,j)$ in the following schematic representation collocated control volume equations:

$$\begin{aligned} u(i,j,k,n+1) &= u(i,j,k,n) + \Delta t * [U(i,j,k) + f * v + uz], \\ v(i,j,k,n+1) &= v(i,j,k,n) + \Delta t * [V(i,j,k) - f * u + vz]. \end{aligned} \tag{12}$$

The usual two-point representation of the pressure gradient terms PX and PY in U and V would be as follows:

$$\begin{aligned} PX(i,j,k) &= [p(i+1,j,k,n+1/2) - p(i-1,j,k,n+1/2)]/(2 * \Delta x) \\ PY(i,j,k) &= [p(i,j+1,k,n+1/2) - p(i,j-1,k,n+1/2)]/(2 * \Delta y) \end{aligned} \tag{13}$$

In the spirit of improving the accuracy of important terms and to have a fairer comparison with the staggered 'c'-grid Schemes 1B and 2B, the following relations are used in Scheme 3B instead of (13):

$$\begin{aligned} PX(i,j,k) = \{&10 * [p(i+1,j,k,n+1/2) - p(i-1,j,k,n+1/2)] \\ &- [p(i+2,j,k,n+1/2) - p(i-2,j,k,n+1/2)]\}/(16 * \Delta x), \\ PY(i,j,k) = \{&10 * [p(i,j+1,k,n+1/2) - p(i,j-1,k,n+1/2)] \\ &- [p(i,j+2,k,n+1/2) - p(i,j-2,k,n+1/2)]\}/(16 * \Delta y). \end{aligned} \tag{14}$$

2. Integrate the full equations (12), including the implicitly coupled Coriolis and vertical diffusion terms, at the p-locations:

$$\begin{aligned} u(i,j,k,n+1) = u(i,j,k,n) &+ \Delta t * [U(i,j,k) \\ &+ f * v(i,j,k,n+1) + uz(i,j,k,n+1)], \\ v(i,j,k,n+1) = v(i,j,k,n) &+ \Delta t * [V(i,j,k) \\ &- f * u(i,j,k,n+1) + vz(i,j,k,n+1)]. \end{aligned} \tag{15}$$

3. Interpolate the new velocity to the staggered 'c'-grid advection velocity positions using four-point interpolations. Letting $u(i,j)$ and $v(i,j)$ represent $u(i,j,k,n+1)$ and $v(i,j,k,n+1)$ as calculated in equation (15), these interpolations can be written as follows:

$$\begin{aligned} u(i+1/2,j) &= \{9*[u(i,j)+u(i+1,j)]-[u(i-1,j)+u(i+2,j)]\}/16, \\ u(i-1/2,j) &= \{9*[u(i-1,j)+u(i,j)]-[u(i-2,j)+u(i+1,j)]\}/16, \\ v(i,j+1/2) &= \{9*[v(i,j)+v(i,j+1)]-[v(i,j-1)+v(i,j+2)]\}/16, \\ v(i,j-1/2) &= \{9*[v(i,j-1)+v(i,j)]-[v(i,j-2)+v(i,j+1)]\}/16. \end{aligned} \tag{16}$$

4. Clear out the divergence of the vertically averaged advection velocity calculated in step 3 using exactly the same procedure as described in step 5 for Scheme 1A (see Section 3.1). The resulting non-divergent velocity could be interpolated back to the collocated locations, but this dissipative step is not performed in this study.

Steps 5 and 6 correspond exactly to steps 6 and 7 for Scheme 1A (see Section 3.1).

Note that the interpolations in step 3 are non-dissipative, since interpolations back to the collocated positions are not performed.

Two advantages to Scheme 3B are: it is somewhat simpler than the others since the convection and diffusion terms have the same form for all quantities; and the implementation of general boundary-fitted co-ordinates is considerably simplified. However, the results below suggest that this higher-order interpolation collocated approach is slightly less accurate than the similarly higher-order interpolation 'c'-grid approaches (Schemes 1B and 2B). This is probably related to the fact that the fourth-order pressure gradient must be evaluated over four grid intervals (a second-order scheme would be much less accurate), while the four-point interpolations on the 'c'-grid interpolate data over only three grid intervals.

3.5. Energy conservation considerations

Conservation of any quantity is a virtue for a numerical method. Energy conservation by the convective terms is considered particularly desirable in modelling geophysical flows,[11] since this avoids build-up of aliasing effect that can lead to non-linear instability.[12] Such non-linear instability can be suppressed by using sufficiently large eddy diffusivity coefficients that the cell Reynolds number[9] does not exceed $O(1)$ anywhere. However, this is inadequate for modelling geophysical flows owing to the occurrence of significant eddies that behave in a nearly inviscid manner and have not been successfully parametrized by any turbulence closure scheme. If adequate turbulence closure schemes are not available, it is desirable in general to use numerical schemes that are stable (avoid non-linear instability) when the cell Reynolds number is large. Even if the physical dissipative scales could be barely resolved, the cell Reynolds number would have to be $O(1000)$ to model them, because they are the result of instabilities that occur only at large Reynolds number.

Although Schemes 1A and 1B described above do not maintain the finite difference analogue of the aforementioned desirable energy conservation property, the results discussed in Section 4 below suggest they are just as accurate and robust as the corresponding Schemes 2A and 2B, which do maintain such conservation, as we now further discuss.

All five schemes described above use a finite difference scheme for the convection terms that is of the conditional energy-conserving class described in Reference 13, the condition being that the finite volume incompressibility integral condition be exactly satisfied for the smallest grid elements. All five schemes satisfy this incompressibility condition to a tight tolerance and this

naturally applies to the smallest resolved grid elements owing to the 'c'-grid staggering of the non-divergent advective velocity.

The conservative schemes[13] are exactly conservative except for the time truncation error, but this is not involved in the non-linear instability problem described in Reference 12. If desired, a modified trapezoidal time integration method can be used together with Bryan's spatially conservative schemes to get exact energy conservation,[14] but this is often considered as not worth the extra computation required.

However, interpolation of intermediate momentum results between the scalar pressure locations and the staggered velocity locations is done within each time step by the four 'c'-grid schemes (1A, 1B, 2A and 2B) described above. Interpolation is needed to integrate the Coriolis terms on a 'c'-grid. The particular interpolation approaches of these four schemes are preferred owing to their facilitating efficient, accurate boundary layer modelling.[1] They are also excellent schemes more generally, as the results in Section 4 show. While the interpolation approaches of Schemes 2A and 2B retain the energy conservation property, those of Schemes 1A and 1B do not (contrary to our claim in Reference 1). However, in spite of the resulting potential non-linear instability, the non-conservative Schemes 1A and 1B are numerically stable for extremely low diffusivities, as noted by Ezer[3] and also indicated by the results in Section 4.1 below, and in fact appear at least competitive with their exactly conservative counterparts, Schemes 2A and 2B.

In fact, the low horizontal diffusivities used by Scheme 1B in generating the results shown in Section 4.1 below are at least 1000 times smaller than we found were required for numerical stability using the Bryan–Semtner model[15] in a rectangular flat-bottom basin calculation patterned after the North Atlantic Ocean using 200 km resolution.

Furthermore, Scheme 1B is currently being applied to the calculation of the circulation of the North Atlantic Ocean using real topography, realistic surface layer heating and wind stress driving and 50 km resolution. In this calculation constant vertical diffusivity of $1\ \mathrm{cm^2\,s^{-1}}$ is being used, with no special convective adjustment other than what is calculated naturally from the full hydrostatic equations. Owing to the low numerical dissipation of SOMS, the calculated flow overturns naturally (as it should) on the smallest resolved scale in convectively unstable regions, yet the largest vertical velocities are less than $0{\cdot}1\ \mathrm{cm\,s^{-1}}$, with typical values being $O(0{\cdot}01\ \mathrm{cm\,s^{-1}})$ outside convectively unstable regions.

Thus it appears that the lack of exact energy conservation by Schemes 1A and 1B does not lead to non-linear instability. This is not too surprising in view of the generally dissipative nature of interpolations, which are the only cause of lack of exact energy conservation in these schemes.

The fact that hydrostatic models using the conservative schemes[13] conserve kinetic energy only for the horizontal velocity does not affect their avoidance of non-linear instability. The incompressibility condition limits the vertical velocity for a given horizontal velocity, especially with the thin-shell nature of geophysical flows (which itself is needed for hydrostatic models to be valid). The effects of rotation and stratification further reduce the vertical velocity below this limit.

4. RESULTS

Contour plots are used extensively in this section. Mid-range contours are dashed with short dashes (25% solid). A dashed 'zero line' is also drawn in some cases and labelled 'Z'; its dashes are generally longer (50% solid). Although the zero line appears on the pressure plots, it has little significance owing to the arbitrary mean value of pressure, which varies with time and can be different with different resolutions. Since the mean pressure is meaningless, only the difference between maximum and minimum pressure is given in the pressure plots. In each plot an 'H' is printed at the maximum and an 'L' is printed at the minimum.

Ten contour intervals are used for the horizontal plots, six for the vertical cross-sections. Contour levels 'N' in the horizontal plots represents values equal to the plot minimum plus 'N' tenths of the difference between the plot maximum and plot minimum. Thus the dashed mid-range contour is labelled '5' in the horizontal plots. The vertical plots have only six contour intervals, so the dashed mid-range contour is labelled '3'. The tick marks at the boundaries of the horizontal plots show the horizontal resolution used.

4.1. The effect of horizontal eddy diffusivity

Three simulations of the test problem described in Section 2 were made with everything fixed except the horizontal heat and momentum diffusivities. They were 10^7, 10^6 and 10^5 cm s^{-1}. The last one yields a flow with cell Reynolds numbers larger than 2000.

Here we show the results from Scheme 1B with these three diffusivities. Later we compare results of the various schemes with various resolutions (Section 4.2).

Runs were made with and without a weak filter[7] applied to the initial surface pressure guess. Such a filter reduces the two-grid-interval oscillation that can occur with Schemes 1A and 1B without the filter. This guess is later replaced by a corrected surface pressure in the calculation procedure. The results (Figures 2 and 3) show that this filter has little effect other than reducing the two-grid-interval oscillation. The two-grid-interval oscillation also decreases as the resolution increases. Schemes 2A and 2B have no tendency for such oscillations, but we prefer Schemes 1A and 1B (see Appendix). The two schemes converge to the same results both here and in Section 4.2.

These results show little difference between the cases with 10^5 and 10^6 cm^2 s^{-1} diffusivities. However, the case with 10^7 cm^2 s^{-1} has substantially larger eddy scales and dissipates substantially during the 30-day integration, while the other two cases showed much less dissipation (Figure 3).

4.2. Convergence with increasing resolution

In convergence tests it is prudent to avoid large cell Reynolds numbers in order for a viscous cut-off to operate on adequately resolved modes. Yet, for best geophysical relevance, the viscosity should not be so large as to stabilize all resolved eddies that would be baroclinically unstable in the absence of viscosity. These considerations led us to choose horizontal heat and momentum diffusivities of 10^7 cm^2 s^{-1} in the convergence tests.

In the convergence test sequences, everything is fixed except the time and space resolution. Three resolutions are calculated for all five schemes described in Section 3. The horizontal grid intervals are respectively 40, 20 and 10 km (corresponding to 15 × 12, 30 × 24 and 60 × 48 horizontal grids). The time step sizes are respectively 60, 30 and 15 min. The vertical resolutions are respectively three, seven and 15 layers, except as noted.

The three resolutions diverge as time progresses until the available potential energy is dissipated and the flow becomes wind-dominated. This is true in general for flows dominated by free modes resulting from instabilities. However, the results show that convergence is achieved up to 30 days, which is remarkable in view of the thin boundary layers that develop immediately and remain throughout the calculation.

We first show results from three resolutions using Scheme 2B. We then compare the converged results (10 km resolution) with results from the other four schemes described in Section 3. Results from all calculations are summarized in Section 4.3.

Figure 4 shows the mid-depth pressure (left) and barotropic streamfunction (right) at 30 days, from 40, 20 and 10 km resolution calculations using Scheme 2B. (We chose the mid-depth

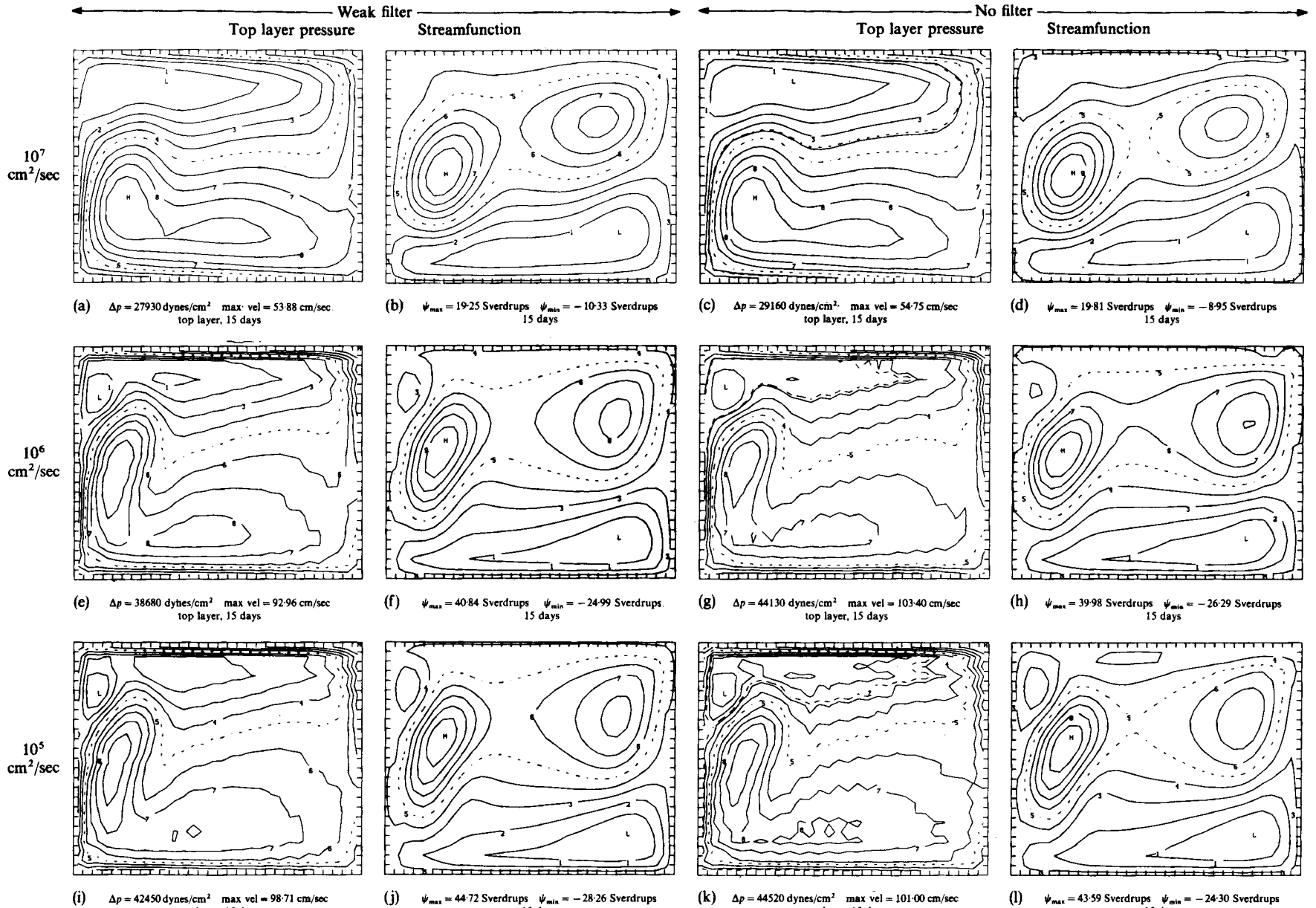

Figure 2. Effect of diffusivity and filter: results at 15 days

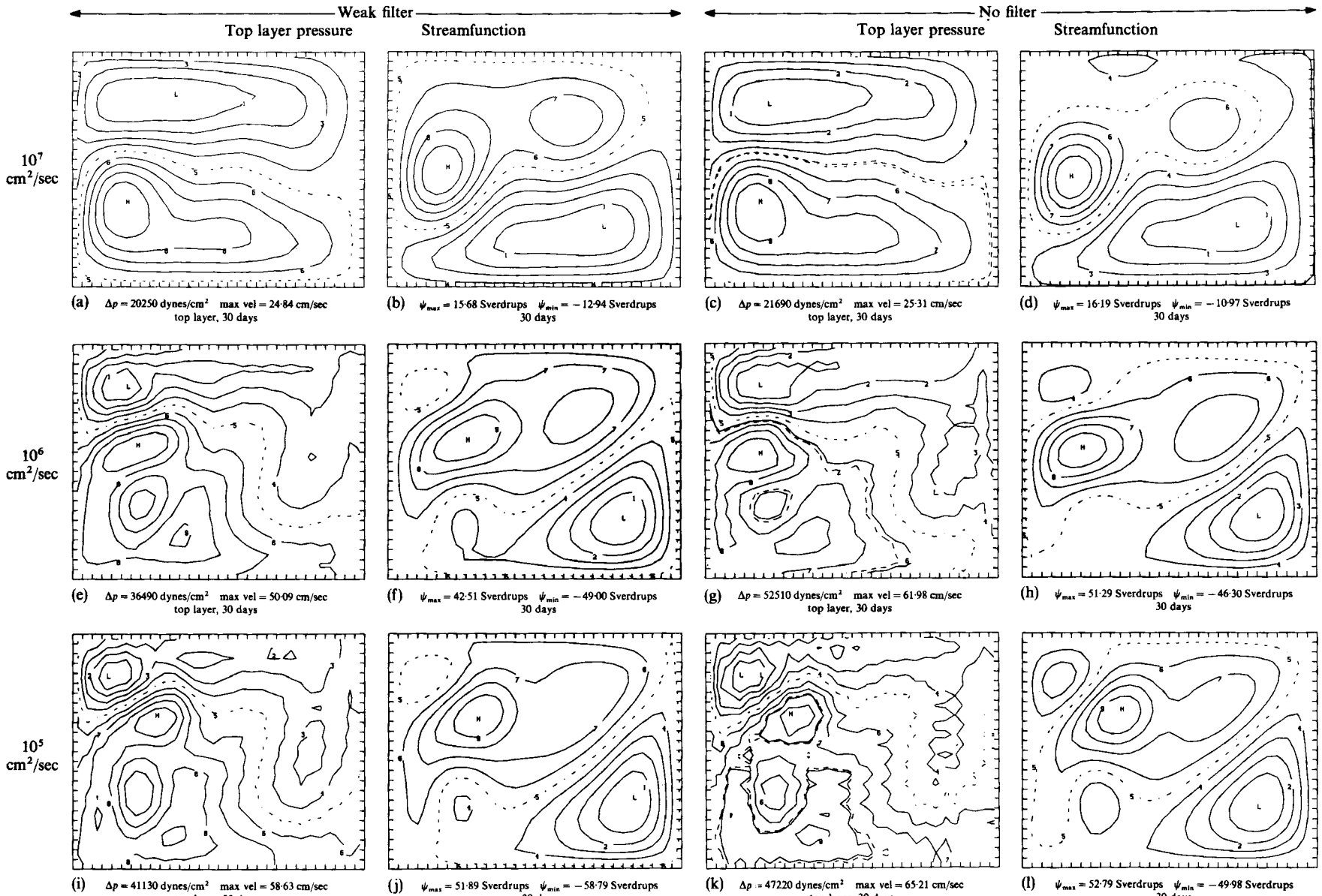

Figure 3. Effects of diffusivity and filter: results at 30 days

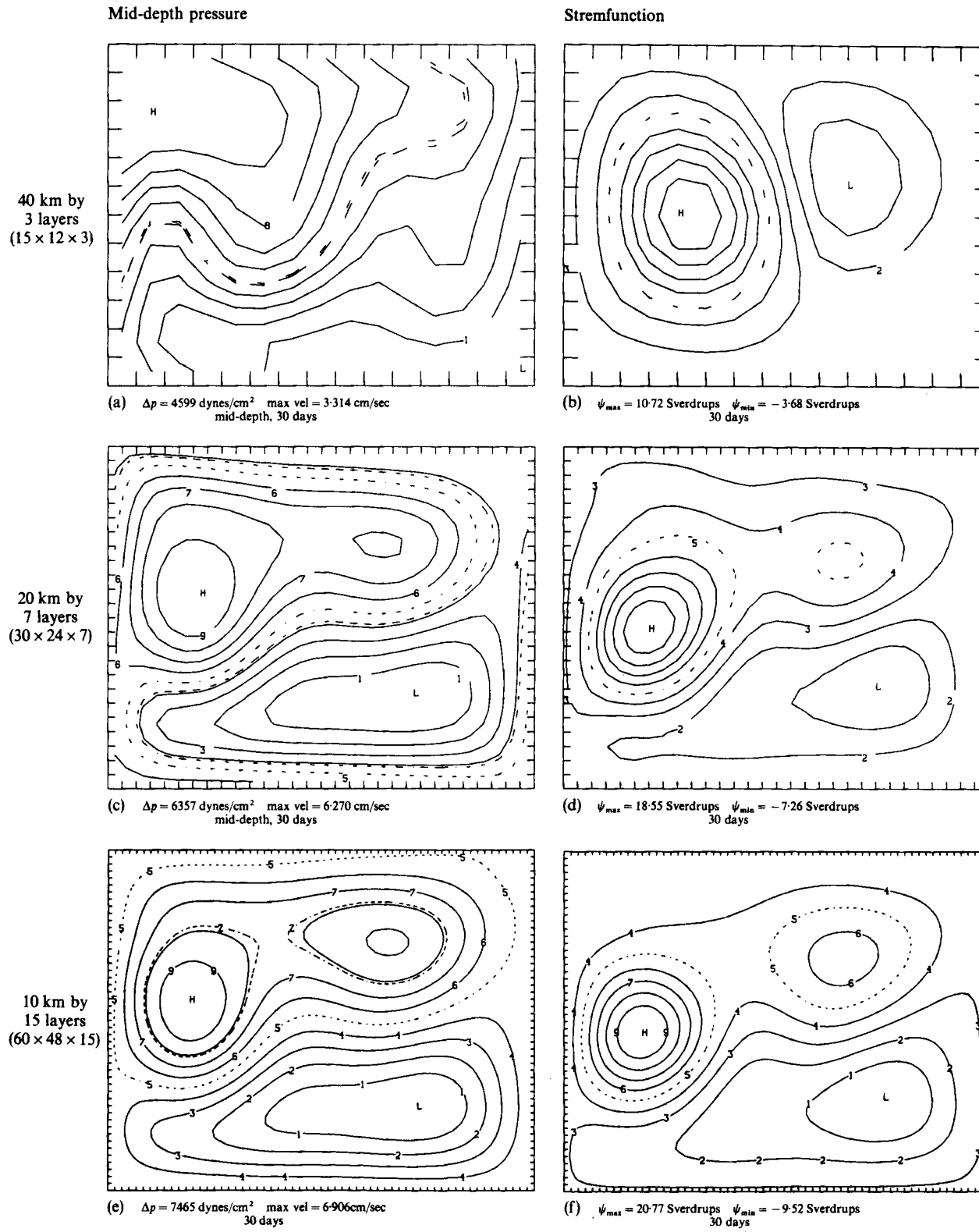

(a) $\Delta p = 4599$ dynes/cm^2 max vel = 3·314 cm/sec mid-depth, 30 days

(b) $\psi_{max} = 10{\cdot}72$ Sverdrups $\psi_{min} = -3{\cdot}68$ Sverdrups 30 days

(c) $\Delta p = 6357$ dynes/cm^2 max vel = 6·270 cm/sec mid-depth, 30 days

(d) $\psi_{max} = 18{\cdot}55$ Sverdrups $\psi_{min} = -7{\cdot}26$ Sverdrups 30 days

(e) $\Delta p = 7465$ dynes/cm^2 max vel = 6·906cm/sec 30 days

(f) $\psi_{max} = 20{\cdot}77$ Sverdrups $\psi_{min} = -9{\cdot}52$ Sverdrups 30 days

Figure 4. Effect of resolution: Scheme 2B, results at 30 days

pressure here because, in contrast to the calculations shown in Figures 2 and 3, the vertical resolution variation in these convergence tests changes the vertical location of the top layer pressure. Since an odd number of uniform thickness layers is used in all three resolutions, mid-depth pressure is best for showing convergence.) Owing to the effects of the dissipative interpolations, the 40 km calculation shows less energy and larger-scale eddies than the more accurate 20 and 10 km calculations. The relatively small difference between the 20 and 10 km calculations indicates convergence.

The main difference between the results with 20 km resolution and with 10 km resolution in Figure 4 is due to the increased horizontal resolution rather than vertical, although the 10 km case has 15-layer vertical resolution compared to the seven-layer vertical resolution used in the 20 km case. This is shown by comparison with Figure 5, which uses 10 km horizontal resolution and seven layers. The Figure 5 results are much closer to the 10 km results in Figure 4 than to the 20 km results. This is not surprising in view of the relatively simple vertical structures in the converged solutions (see Figure 9 below). These simple structures result in spite of the very low vertical diffusivities used.

Figure 6 shows the top layer pressure at 15 days with the various resolutions. Note that Figures 6(c) and 6(d) are nearly identical. This is due to the fact that vertical variations are well resolved in both calculations.

Figure 7 compares the converged solutions (10 km resolution for the five schemes described in Section 3. Top layer pressure (left), temperature (middle) and barotropic streamfunction (right) are shown at 30 days. Note that the three higher-order interpolation schemes have converged to almost the same result. The low-order Scheme 1A compares more favourably at 15 days, as shown by Figure 8. The deterioration of Schemes 1A and 2A relative to the others between 15 and 30 days is due to their lower-order interpolations and associated increased numerical dissipation.

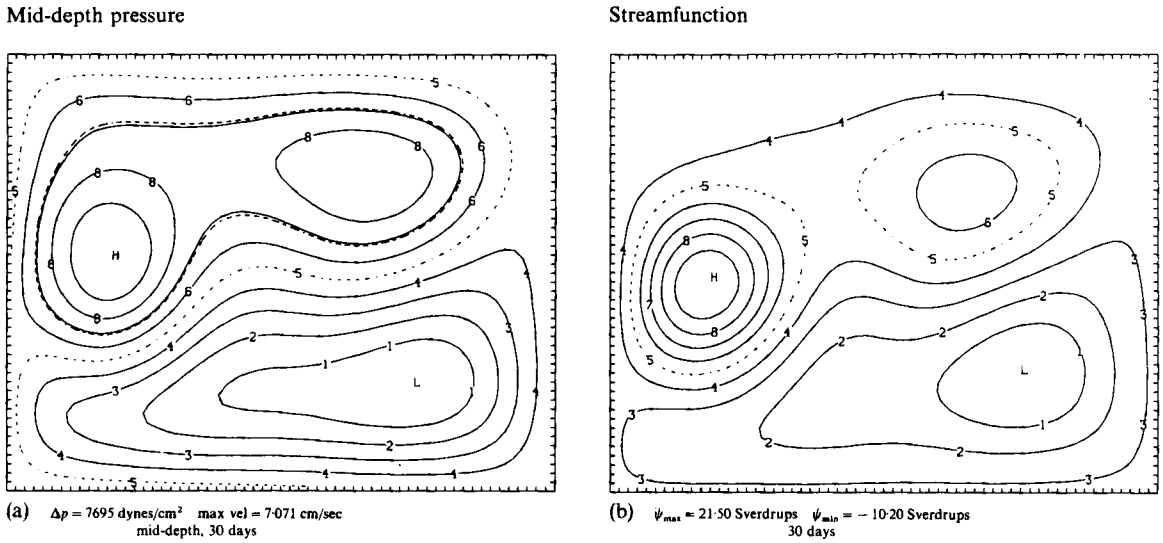

Figure 5. Effect of resolution: Scheme 2B, results at 30 days. Comparison with Figure 4 shows that seven layer vertical resolution is adequate for the flat-bottom calculations performed

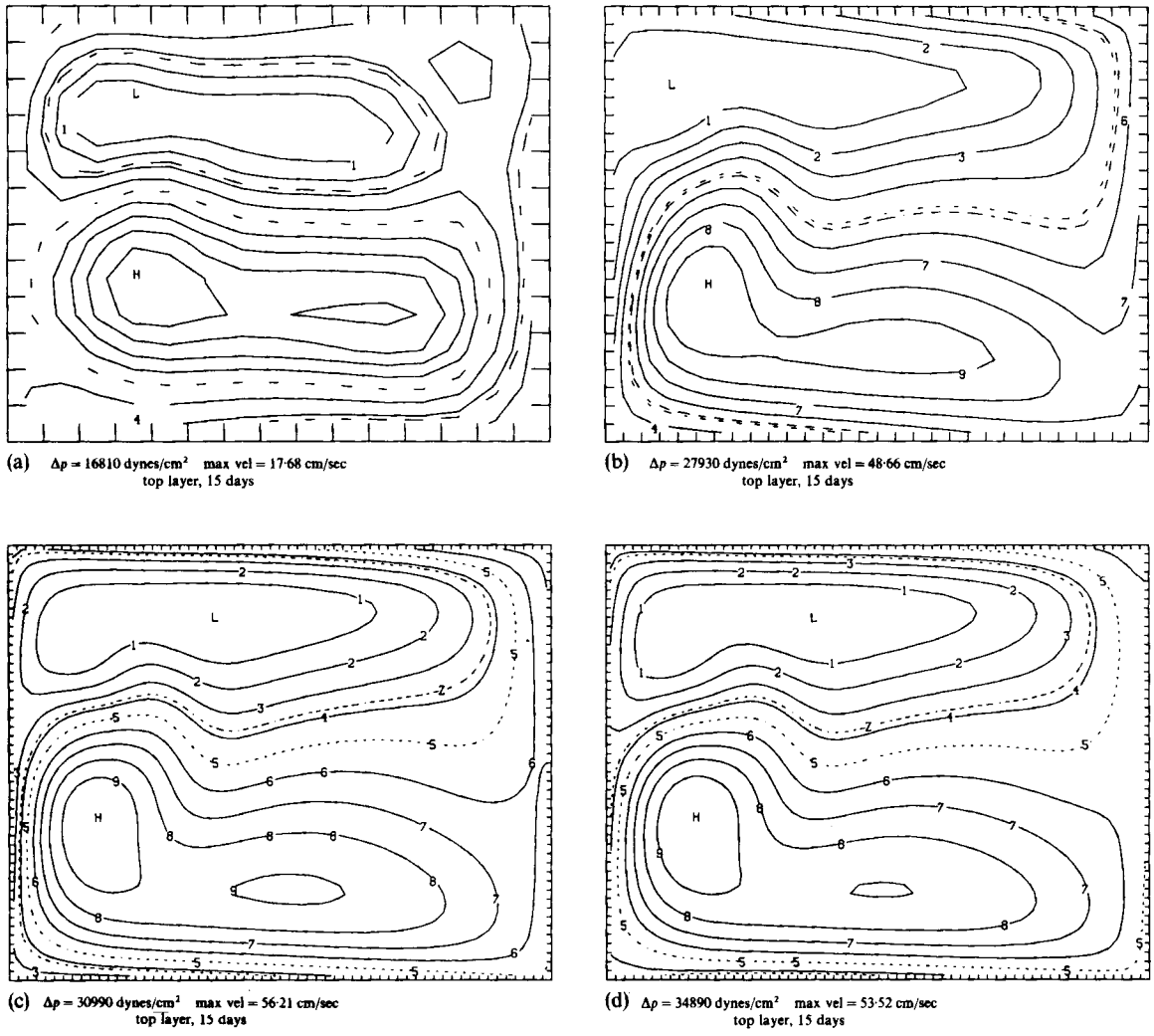

Figure 6. Effect of resolution: Scheme 2B, results at 15 days. Top layer pressure. Comparison of plot (d) with plots (b) and (c) further demonstrates that seven layer vertical resolution is adequate for the flat-bottom calculations performed. (a) 40 km by three layers (15 × 12 × 3); (b) 20 km by seven layers (30 × 24 × 7); (c) 10 km by 15 layers (60 × 48 × 15); (d) 10 km by seven layers (60 × 48 × 7)

Figure 9 shows that even vertical velocity is similar for the higher-order interpolation calculations. It is not as well converged as the other fields. This is due to the relative importance of fine structures in the vertical velocity field. (Although SOMS is a full primitive equation model, the horizontal flow component in the test problem is quasi-non-divergent. It follows that its vertical velocity could be approximated by solving the quasi-geostrophic omega equation,[16] whose forcing is dominated by non-linear terms, in contrast to the horizontal momentum equations, which are dominated by a linear quasi-geostrophic balance. This, of course, leads to finer structures.)

Although vertical velocity is only $O(0{\cdot}1\ \mathrm{mm\,s^{-1}})$, it is important to address it realistically in many applications. In spite of their very low energy levels, vertical overturnings release potential

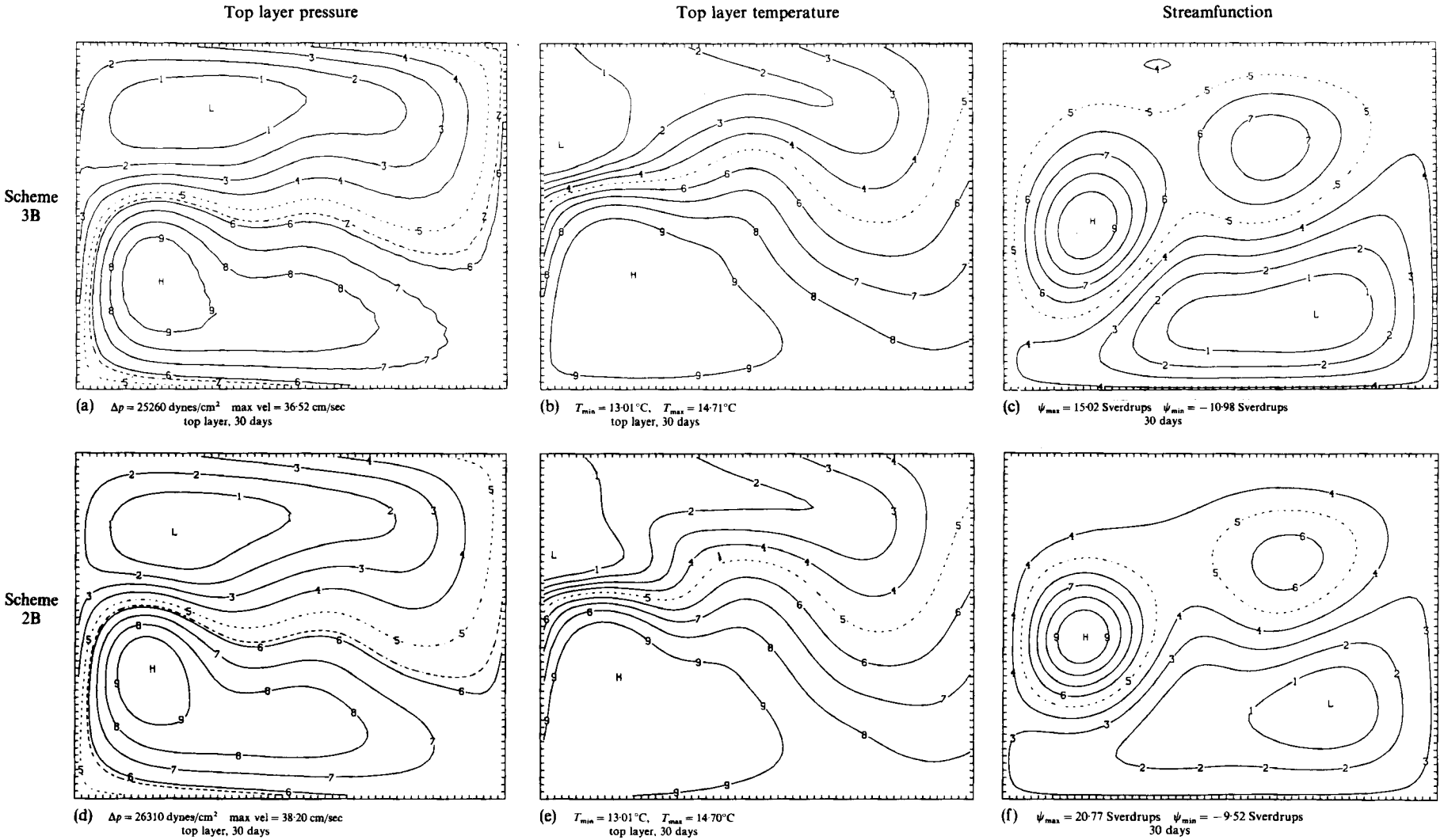

Figure 7. Results at 30 days from the five schemes with 10 km by 15-layer resolution. Schemes 1A and 2A are less well converged owing to their lower-order (two-point) interpolations

(Figure 7 is continued overleaf)

Scheme 1B

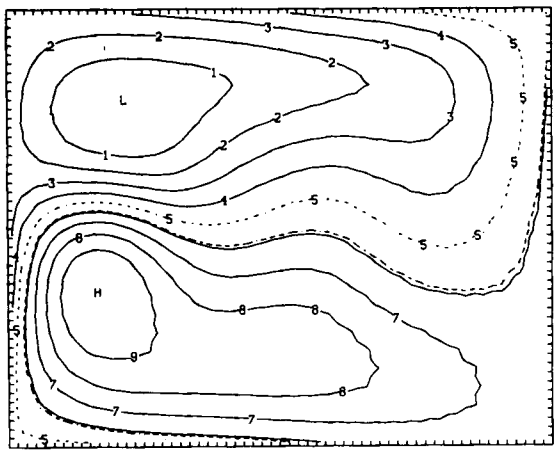

(g) $\Delta p = 27280$ dynes/cm^2 max vel = 41·54 cm/sec
top layer, 30 days

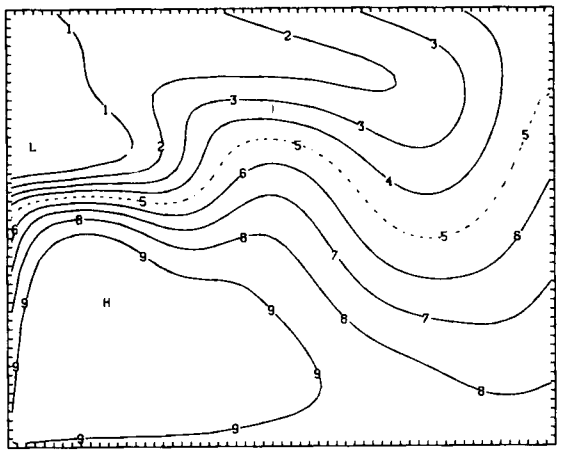

(h) $T_{min} = 13{\cdot}05$°C, $T_{max} = 14{\cdot}70$°C
top layer, 30 days

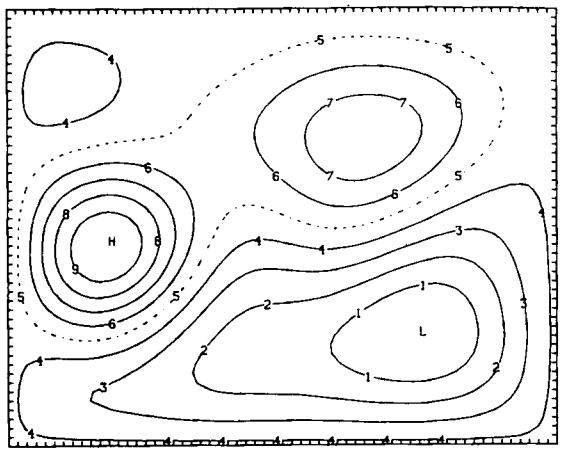

(i) $\psi_{max} = 18{\cdot}81$ Sverdrups $\psi_{min} = -13{\cdot}97$ Sverdrups
30 days

Scheme 1A

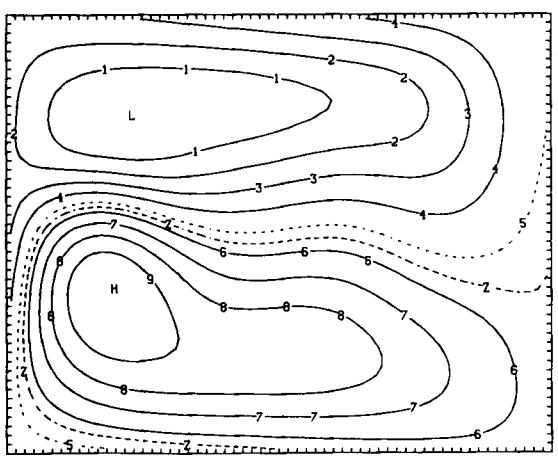

(j) $\Delta p = 18042$ dynes/cm^2 max vel = 30·87 cm/sec
top layer, 30 days

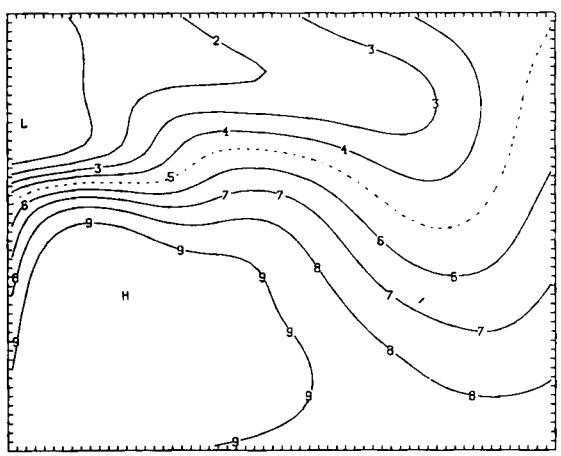

(k) $T_{min} = 12{\cdot}98$°C, $T_{max} = 14{\cdot}70$°C

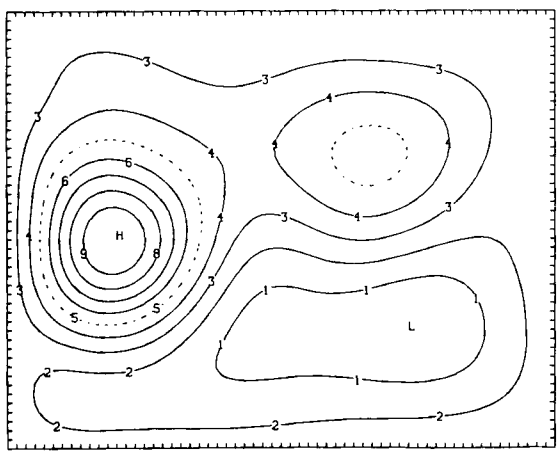

(l) $\psi_{max} = 16{\cdot}57$ Sverdrups $\psi_{min} = -5{\cdot}23$ Sverdrups
30 days

Figure 7. (Continued)

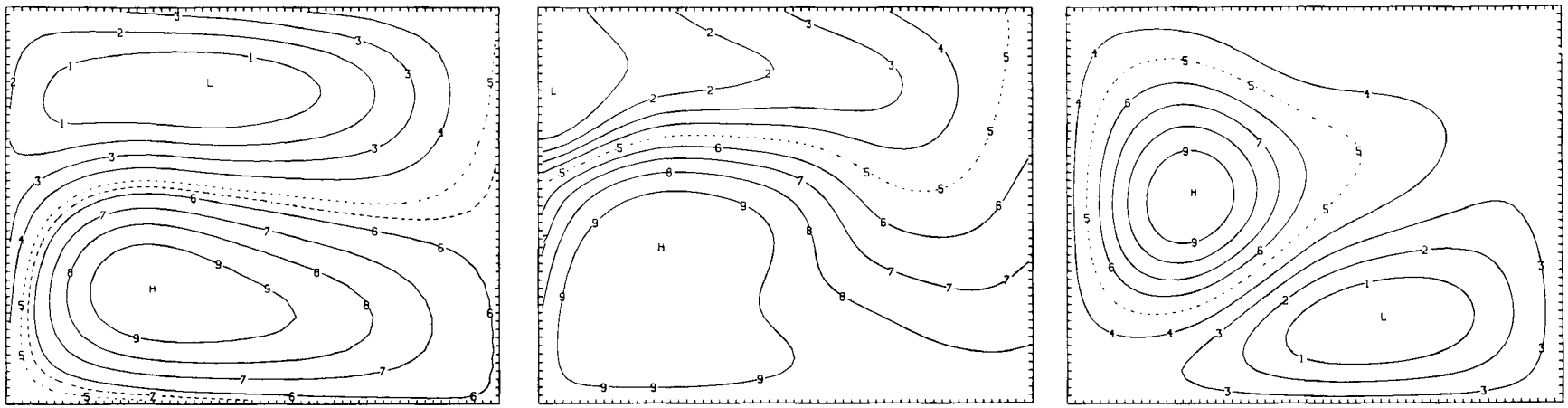

(m) $\Delta p = 22240$ dynes/cm^2 max vel = 20·79 cm/sec
top layer, 30 days

(n) $T_{min} = 12{\cdot}95°C$, $T_{max} = 14{\cdot}72°C$
top layer, 30 days

(o) $\psi_{max} = 4{\cdot}305$ Sverdrups $\psi_{min} = -2{\cdot}353$ Sverdrups
30 days

Figure 7. (Concluded)

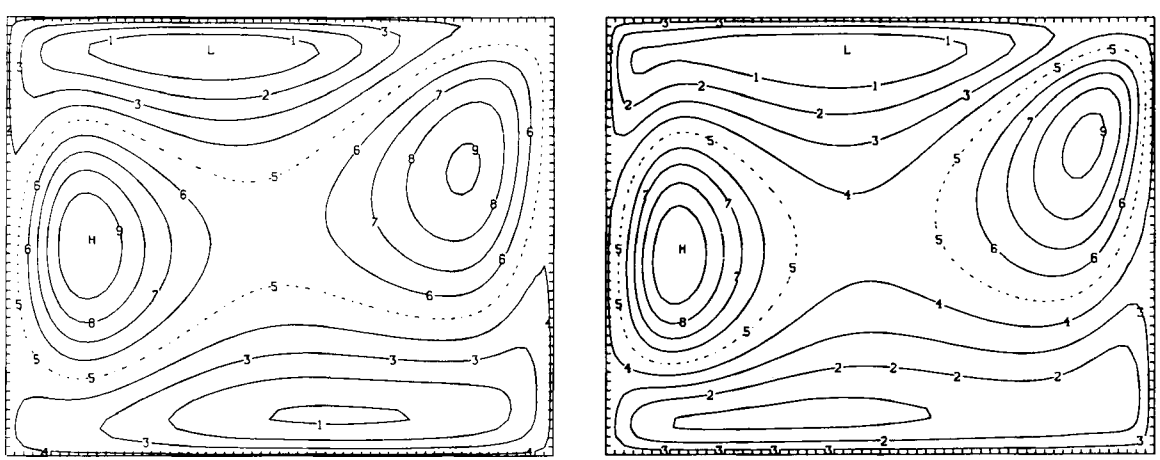

(a) $\psi_{max} = 13{\cdot}28$ Sverdrups $\psi_{min} = -9{\cdot}82$ Sverdrups
15 days

(b) $\psi_{max} = 19{\cdot}81$ Sverdrups $\psi_{min} = -11{\cdot}96$ Sverdrups
15 days

Figure 8. Results at 15 days from Schemes 1A and 1B with 10 km by 15-layer resolution. Streamfunction plots show much closer agreement than at 30 days (see Figure 7)

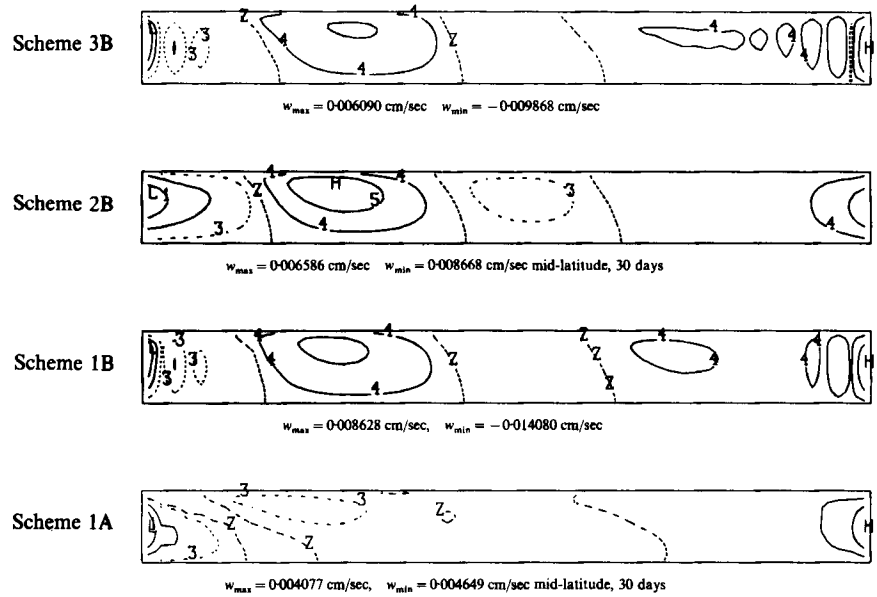

Figure 9. Vertical velocity plots at 30 days from the five schemes with 10 km by 15-layer resolution. Mid-latitude plots of vertical velocity are similar to one another, especially for the more accurate calculations (3B, 2B and 1B)

energy generated by horizontally differential heating, and thus are a major force in driving ocean general circulations. They also are important in the many environmentally important processes that are controlled by vertical mixing rates.

4.3. Summary of the convergence results

In Section 4.2, convergence in detail was demonstrated for the five schemes tested by showing contour plots at various times. We now compare these schemes in terms of their general properties.

Figure 10 summarizes the relative behaviour of the schemes. Time plots of the root-mean-square velocity (in $cm\,s^{-1}$) during the 30-day integration are shown for each scheme.

Figure 10(a) shows the time variations of the converged solutions (10 km resolution) for the three most accurate schemes (four-point interpolations). This verifies that the semi-collocated grid approach, Scheme 3B, as incorporated into SOMS, is competitive with the more popular Arakawa 'c' staggered grid approaches. However, this figure indicates that Scheme 3B has slightly larger damping than the other two high-order interpolation schemes (1B and 2B). This increased damping is even more evident by comparing Scheme 3B with Schemes 1B and 2B in calculations with smaller diffusivities and, correspondingly, less physical damping (not shown).

Figures 10(b)–10(d) show the relatively rapid and complete convergence of the schemes using higher-order interpolations, Schemes 3B, 2B and 1B. Figures 10(e) and 10(f) show the relatively slow and incomplete convergence of the two schemes using lower-order interpolations, Schemes 2A and 1A. Figures 10(g) and 10(h) compare the low (40 km) and intermediate (20 km) resolution results of the various schemes with the high (10 km) resolution converged result from Scheme 1B. These plots show that, for the geophysical prototype problem simulated, the more accurate schemes (1B and 2B) produce better results (with substantially less damping) using 20 km resolution than those produced by the corresponding less accurate schemes (1A and 2A) using 10 km resolution.

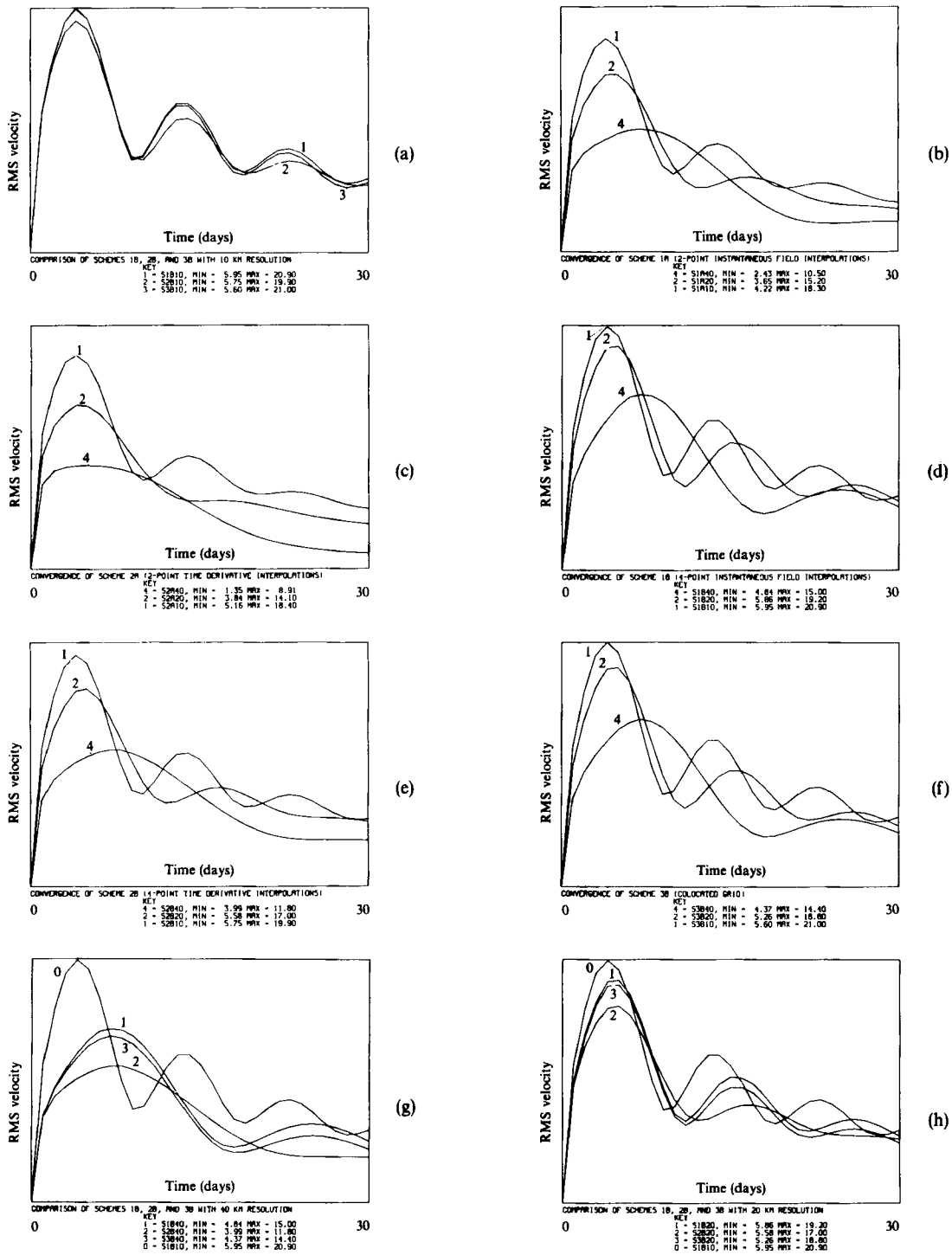

Figure 10. General comparison of the five schemes. The time dependence of the RMS velocity (averaged over the whole model region) is shown for the five schemes (1A, 2A, 1B, 2B and 3B) described in Section 3, using 10, 20 and 40 km resolutions, and applied to the geophysical prototype problem described in Section 2. The simulations covered 30 model days and were all performed on a Vax 8700, with the highest resolution (2880 time steps on a 62 × 48 × 15 grid) requiring about 460 min CPU time. Units are cm s^{-1}. The naming convention used in the keys is illustrated by one example: S1B20 is the calculation using Scheme 1B with 20 km resolution

In summary, these results show that the new, more accurate treatments of the Coriolis and pressure gradient terms, which generally dominate geophysical flows, provide converged solutions with lower resolution and, correspondingly, less computation than required by the lower-order interpolation treatments of the classical approaches, including the treatment used by the Bryan–Semtner–Cox (BSC) model,[17] which is the most widely used model corresponding to SOMS (but does not include the SOMS advanced bottom boundary layer treatment).

This is particularly significant in view of the high cost of modelling ocean-scale flows: 250 h of dedicated Cray-XMP/48 time were used by the BSC for 20 years of world ocean simulation, using all CPUs almost all of the time (99·64% according to Reference 17). The BSC calculation apparently used a split time step approach during the first 18 years, which saves about a factor-of-seven computing time.[17] This split time step approach involved using a time step for the momentum transport equation that is 49 times shorter than the time step for the density transport equation, while taking only one momentum equation time step per density equation time step. A matched time step was used only during the last two years, which took 100 h of the 250 h total.

For comparison, with a matched time step SOMS requires about 33 min of CPU on a Cray 1 computer per model year when 50 km resolution and 12 layers are used in a North Atlantic calculation (with maximum depth 6000 m and a 67 × 74 horizontal grid). On the basis of the factor-of-eight increased speed of the Cray-XMP/48 calculation used by the BSC compared to a Cray 1, the BSC would require about 333 min of CPU per model year for a similar North Atlantic calculation. This comparison has about a factor-of-two uncertainty, mainly owing to uncertain time step size limits; however, it is close to the more carefully determined factor-of-10 reduced cost by SOMS reported in Reference 1, even though the BSC has now been thoroughly optimized.

It should be noted that the aforementioned BSC split time step approach provides a Rossby radius of deformation[16] that is seven times its correct physical value. This Rossby radius of deformation is the distance an internal wave propagates during one inertial period (associated with the Coriolis parameter, about 18 h in mid-latitudes), which depends on two very dominant effects: buoyancy and Coriolis acceleration. The most unstable baroclinic eddies have scales proportional to this parameter.[16] In the ocean this scale is a few hundred kilometres.

Not surprisingly, when we tried the BSC split time step approach on the geophysical prototype problem described in Section 2, the converged flow regime was entirely different from the converged solutions shown in Section 4.2. Thus for flows with significant baroclinic eddies we do not recommend this split time approach used in the BSC calculation.[17] We also believe that the BSC results[17] are further compromised by their use of a smoothing scheme based on the biharmonic operator.

In comparison with BSC the SOMS results consistently demonstrate better numerical performance (lower numerical dissipation, lower cost for the same resolution). The SOMS accuracy is further enhanced by using the higher-order interpolations of Schemes 1B, 2B and 3B in this study. Analagous higher-order interpolations would no doubt also benefit the BSC.

We suspect that the popular 'c'-grid is a major factor in the better performance by SOMS. It is well known that the 'c'-grid is better than the 'b'-grid for processes involving the pressure gradient terms, including those involving internal wave propagation in the ocean. In geophysical models it is also known that the 'b'-grid used by the BSC model is at least competitive with the classical 'c'-grid approach when the grid interval is large compared to the Rossby radius of deformation, which is O(50–100 km) in the ocean. We have found SOMS to have major advantages compared to the BSC, even for 200 km resolution, owing to the large diffusivities and small time step required by the BSC for stability.[1] For more details on the comparison between the BSC 'b'-grid and the classical 'c'-grid approaches, see References 18–21. The modified 'c'-grid approaches used by SOMS in this study have not been analysed in such detail. However, convergence studies such

as performed here are adequate in themselves for comparison of various grids and numerical approaches, and have not been published for other models.

4.4. The northern basin gyre

Figure 8 shows a cyclonic gyre near the northern boundary. This can be explained as follows. Early in time, the cold northern basin water results in generally low pressure near the top, with positive vorticity generated by horizontal convergence associated with sinking cold water, and high pressure near the bottom, with negative vorticity generated by horizontal divergence. There is an associated meridional circulation of northward zonally averaged flow in the upper levels and southward zonally averaged flow in the lower levels. Thus there is a net vertically averaged cyclonic vorticity transport northwards, across intermediate latitudes, into the northern region. Since all physical boundaries are closed, this means there is a net (vertically averaged) positive vorticity accumulation in the northern region. This effect decreases as the isotherms flatten out in this model problem (there is no latitudinal differential heating to maintain the initial baroclinicity or horizontal density gradients), so the northern barotropic cyclonic gyre decreases later in time, as Figure 7 shows. Bottom friction sinks for negative vorticity would reinforce this effect but are probably quite secondary.

This mechanism also creates a barotropic cyclonic circulation near the southern boundary of the basin. The combined effect of the southward transport of positive vorticity near the southern boundary and the northward transport near the northern boundary creates a mid-basin barotropic anticyclonic circulation independent of wind forcing. The southern and northern barotropic circulations are further enhanced by another non-linear effect in the vertically averaged vorticity equation, owing to a positive correlation of vorticity with convergence.

This generation mechanism for barotropic gyres is a weak secondary effect. In nature this mechanism is maintained by the latitudinal differential heating (the heating term in the omega equation forces large-scale sinking flow in northern basin regions). The gyre amplitudes depend on a balance between gyre dissipation by horizontal diffusion and mixing of the gyre vorticity, and gyre generation by latitudinal differential heating and vorticity exchange at the basin bottom. Thus, in spite of the weak generation mechanism, it could lead to significant barotropic gyres if the gyre dissipation effects are sufficiently weak.

It is likely that in nature the gyre dissipation effects are weaker in the southern part of the North Atlantic than in the northern part, owing to the increased static stability and associated decreased turbulent mixing. The barotropic gyre amplitude (cyclonic near the southern and northern boundaries, anticyclonic at intermediate latitudes) would be affected by these relative dissipation rates along with the relative strengths of the generation mechanisms.

Depending on the relative strengths of these barotropic gyre generation and dissipation mechanisms, boundary currents could be significantly affected, including separation points. However, SOMS application to ocean basin-scale flows[5] suggests these effects are probably secondary compared to thermodynamic driving of baroclinic boundary current components.

5. IMPLICATIONS OF RESULTS

The convergence studies show that the new higher-order interpolation schemes (1B and 2B on the 'c' staggered grid, 3B on the collocated grid) are far more accurate than their lower-order interpolation counterparts (1A and 2A). These schemes increase the calculation per grid point per time step by less than 2% and are easily incorporated into existing programs. (With SOMS it took only a few days.) They are also applicable to the treatment of swirl curvature terms in many swirling flows of engineering interest.

Already having produced realistic results for a wide range of geophysical phenomena, SOMS has now been shown to converge as the resolution increases in a geophysical prototype problem with free modes owing to baroclinic instability. It is a remarkable and regrettable fact that such grid convergence studies, while clearly essential to establishing the reliability of CFD codes,[22,23] are so rare as to be virtually non-existent in the ocean modelling literature (also, as one reviewer noted, in the atmospheric modelling literature). Thirty-day integrations with this geophysical prototype problem show that SOMS is robust, with eddy viscosity at least as low as 10^5 cm^2 s^{-1} with 20 km resolution, corresponding to a cell Reynolds number $O(2000)$. (We are currently calculating North Atlantic Ocean circulation using horizontal and vertical diffusivities of 1 cm^2 s^{-1} and 50 km resolution.) SOMS produces nearly identical results in this problem with an eddy viscosity of 10^6 as with 10^5, but produces larger-scale free modes with much more rapid dissipation when the eddy viscosity is increased to 10^7.

Since the eddies that dominate the ocean general circulation behave in a nearly inviscid manner, it thus appears that eddy viscosities much larger than $O(10^6)$ cm^2 s^{-1}, as often used (e.g. see Reference 17), are inappropriate for general circulation calculations.

It is especially important to have low numerical dissipation when addressing barotropic gyre generation by latitudinal differential heating, since gyre amplitudes due to mechanisms described in Section 4.3 depend strongly on physical dissipation, which should not be contaminated by numerical dissipation.

6. SOMS APPLICABILITY TO CLIMATE MODELLING

A reviewer has questioned the applicability of SOMS to climate modelling, being of the opinion that strict energy conservation is essential for climate studies.

We first note that the classical 'c'-grid scheme used by Arakawa and Lamb[24] is energy-conserving only if the Coriolis terms are solved implicitly using a trapezoidal scheme. However, such implicit solution couples all points in the horizontal plane. This implies that, even though total energy is conserved, unphysical energy dispersion occurs owing to the coupling. All schemes in this study avoid implicit coupling of horizontal points (the coupling is explicit owing to the interpolations) and are more easily solved in practice for accurate and efficient boundary layer treatment.[1]

We also note that the convection and Coriolis terms are in fact strictly energy-conserving for SOMS Scheme 3B (the Coriolis terms are also non-dispersive), yet Schemes 1B and 2B are quite competitive even though they are not exactly energy-conserving.

Further, we note that it is probably more important to conserve mass and density variance owing to the quasi-balance existing between velocity and density fields. These are easily conserved in both the 'c'-grid used by SOMS and the 'b'-grid used by the BSC model.

In view of these points, although the applicability of Schemes 1B and 2B to climate studies has not yet been demonstrated, we do not believe that their lack of strict energy conservation should exclude them from consideration.

Finally, it is clear that vertical mixing is important to climate modelling and this is dominated by small-scale eddy activity which demands high resolution to model realistically. For modelling such eddies, 'c'-grids such as used by SOMS are preferred.

Thus we believe that our schemes, and SOMS itself, are applicable to climate modelling.

ACKNOWLEDGEMENTS

We gratefully acknowledge stimulating discussions with W. F. Simmons (consultant) and Eduard Zuur (Groupe Prosper, University of Neuchatel, Switzerland), and several helpful comments from

a reviewer. This work was done for U. S. Department of Energy under contract DE-AC04-76DP0079 and for Sandia Contract # 55–5880.

APPENDIX: INTERPOLATION SCHEME COMPARISONS

Schemes 1 (1A and 1B) described in Section 3 interpolate instantaneous velocities (momenta) back to the staggered 'c'-grid locations after adding the effects of the Coriolis term integrations calculated at the collocated *p*-locations. Schemes 2 (2A and 2B) interpolate only the time derivative due to the Coriolis terms and add these to the remaining time derivative components evaluated at the staggered 'c'-grid momentum locations. (The 'A' schemes use two-point interpolations, the 'B' schemes use four-point interpolations). In view of the peculiar truncation error behaviour of Schemes 1 (see Section 3.1), one might expect Schemes 2 to be superior.

However, we have found that Schemes 2 require a smaller time step than Schemes 1 in order to have numerical stability, and that Schemes 2 strongly damp transient eddy activity, especially poorly resolved flow components.

Transient eddies are important in the ocean circulation, but are difficult to resolve in a general circulation scale model. A major effect of transient eddies is to drive the western boundary current (Gulf Stream), and these eddies are a major part of the ocean's response to latitudinal differential heating. In an ocean basin-scale calculation[10] with realistic heating rate and 75 km resolution, Scheme 2A yields a quasi-steady flow with a strong recirculation eddy along the western boundary, with about 35 Sverdrups (1 Sverdrup $\equiv 10^6\,m^3\,s^{-1}$) western boundary current transport, while Scheme 1A produces a flow with much transient eddy activity and a realistically stronger western boundary current of about 60 Sverdrups. The wind driving alone yields a steady flow with both schemes, with about 22 Sverdrups western boundary current, as theoretically predicted on the basis of the return flow of a Sverdrup interior.

Schemes 1 interpolate only instantaneous fields while Schemes 2 interpolate time derivatives. It is thus not surprising that Scheme 1A does best with transient eddies while Scheme 2A favours steady or slowly varying eddies. However, when the flow is well resolved the two schemes give similar results, as shown in Section 4.

Although it is not clear that Schemes 1 are superior in general, we prefer them over Schemes 2 at this time. This is due to their relative simplicity, their success at modelling such a prominent feature as the western boundary current, even with poor resolution of the dominant transient eddies,[10] and our feeling that small-scale steady eddies (as seen in the time-averaged flow) are probably less important in the ocean general circulation than transient eddies, coupled with the relatively weak damping of transient eddies by Schemes 1 compared to Schemes 2.

Although Schemes 1 fail for sufficiently small time step, they appear superior in the calculations performed by SOMS with reasonable time steps. Optimizing the time step size could be automated by using a dynamic time-stepping algorithm (yet to be implemented). Finally, the semi-collocated Scheme 3B behaves well as $\Delta t \to 0$ and is a more likely candidate for extension to boundary-fitted non-orthogonal co-ordinates, especially if symbolic manipulation techniques[25,26] are utilized to automate sections of the code writing.

REFERENCES

1. D. E. Dietrich, M. G. Marietta and P. J. Roache, 'An ocean modeling system with turbulent boundary layers and topography: numerical description', *Int. j. numer. methods fluids*, **7**, 833–855 (1987).
2. E. A. H. Zuur and D. E. Dietrich, 'The SOMS model and its application to Lake Neuchatel', *Aquatic Sci.*, in the press.
3. T. Ezer, 'A study of the benthic boundary layer associated with the cold filament of the western North Atlantic', *Ph.D. Thesis*, Department of Oceanography, Florida State University, Tallahassee, FL, 1989.
4. G. Weatherly, personal communication, 1988.

5. D. E. Dietrich and M. G. Marietta, North Atlantic by SOMS, to be published.
6. A. Arakawa and V. R. Lamb, 'Computational design of the basic dynamical processes of the UCLA general circulation model', *Methods in Computational Physics, Vol. 17*, Academic Press, New York, 1977, pp. 174–265.
7. *SOMS Users' Manual*, Sandia National Laboratories, Albuquerque, NM, to be published.
8. P. J. Roache and D. E. Dietrich, 'Evaluation of the filtered leapfrog–trapezoidal time integration method', *Numer. Heat Transfer*, **14**, 149–164 (1988).
9. P. J. Roache, *Computational Fluid Dynamics*, Hermosa, Albuquerque, NM, 1976.
10. D. E. Dietrich, P. J. Roache and M. G. Marietta, 'Comparison of integration schemes applied to an ocean-scale domain', to be published.
11. S. A. Piacsek and G. P. Williams, 'Conservation properties of convection difference schemes', *J. Comput. Phys.*, **6**, 392–405 (1970).
12. N. A. Phillips, 'An example of non-linear computational instability', in *The Atmosphere and Sea in Motion*, Rockefeller Institute Press and Oxford University Press, New York 1959, pp. 501–504.
13. K. Bryan, 'A scheme for numerical integration of the equations of motion on an irregular grid free of nonlinear instability', *Mon. Weather Rev.*, **94**, 39–40 (1966).
14. D. Dietrich, 'Numerical solution of fully implicit energy conserving primitive equations', *J. Meteor. Soc. Japan*, **53**, 222–225 (1975).
15. A. J. Semtner, 'An ocean general circulation model with bottom topography', *NTIS PB 276 840*, 1974.
16. J. R. Holton, *An Introduction to Dynamic Meteorology, International Geophysical Series, Vol. 16*, Academic Press, New York, 1972.
17. A. J. Semtner and R. M. Chervin, 'A simulation of the global ocean circulation with resolved eddies', *J. Geophys. Res.*, **93**, 15,502–515,522 (1988).
18. F. Messinger and A. Arakawa, 'Numerical methods used in atmospheric models', *GARP Publ. Ser. No. 17, Vol. 1*, WMO, Geneva, 1976.
19. R. C. Wajsowicz, 'Free planetary waves in finite-difference numerical models', *J. Phys. Oceanogr.*, **16**, 773–789 (1986).
20. R. C. Wajsowicz and A. E. Gill, 'Adjustment of the ocean under buoyancy forces. Part I: The role of Kelvin waves', *J. Phys. Oceanogr.*, **16**, 2097–2114 (1986).
21. R. C. Wajsowicz and A. E. Gill, 'Adjustment of the ocean under buoyancy forces. Part II: The role of planetary waves', *J. Phys. Oceanogr.*, **16**, 2115–2136 (1986).
22. P. J. Roache, K. Ghia and F. White, 'Editorial policy statement on the control of numerical accuracy', *ASME J. Fluids Eng.*, **108**, 2 (1986).
23. P. J. Roache, 'The need for control of numerical accuracy', *AIAA 24th Thermophysics Conf.*, Buffalo, NY, 12–14 June 1989; *AIAA J. Spacecraft Rockets*, in the press.
24. A. Arakawa and V. R. Lamb, *Methods in Computational Physics Vol. 17*, Academic Press, New York, 1977, p. 206.
25. S. Steinberg and P. J. Roache, 'Symbolic manipulation and computational fluid dynamics', *J. Comput. Phys.*, **57**, 251–284 (1985).
26. S. Steinberg and P. J. Roache, 'A toolkit of symbolic manipulation programs for variational grid generation', *AIAA Paper No. 86–0241, AIAA Aerospace Sciences Meeting*, Reno, NV, 6–9 January 1986.